

Isotope evidence for the coupled iron and carbon cycles 1.4 billion years ago

H.J. Wang, Y.T. Ye, Y. Deng, X.M. Wang, E.U. Hammarlund, H.F. Fan,
D.E. Canfield, S.C. Zhang

Supplementary Information

The Supplementary Information includes:

- Geological Background
- Methods
- Table S-1
- Figures S-1 to S-4
- Supplementary Information References

Geological Background

The North China Craton

The North China Craton (NCC) is an old craton with a maximum age of well-preserved gneiss of ~3.8 Ga and an area of $\sim 3 \times 10^6$ km². After the formation of a continental nucleus (>3.3 Ga) and the growth of a massive continental crust (2.9–2.7 Ga) (Jia *et al.*, 2019), the western and eastern blocks of the NCC separately completed micro-block assembly and cratonisation at *ca.* 2.5 Ga. The western and eastern blocks amalgamated along the Trans-North China Orogen (TNCO) to constitute a unified basement at *ca.* 1.85 Ga, eventually forming the present tectonic framework of the NCC (Fig. S-1). The continental growth, assembly and breakup of the NCC from 2.5–1.3 Ga is considered an essential component of the assembly of the Columbia supercontinent (Li *et al.*, 2020).

According to the global paleogeographic reconstruction model for the process of the assembly and breakup of the Columbia supercontinent (Pisarevsky *et al.*, 2014), the NCC was considered to be adjacent to Australia during 1.77–1.41 Ga (Zhang *et al.*, 2017). In addition, putative stratigraphic correlations also provide new evidence that the NCC, Siberia and North Australia might have been neighbours and formed a single large intracratonic basin in the Columbia supercontinent (Mitchell *et al.*, 2021).

The Yanliao Basin

From 1.85–1.80 Ga, the tectonic properties of the NCC shifted from compressional to extensional, and remained so for almost one billion years (1.80–0.80 Ga) or perhaps longer (Zhao and Zhai, 2013). Several rift systems (basins) were

formed successively along the margins of the NCC, including the Xiong'er Basin at the southern margin, the Helan-Jinshan Basin at the southwestern margin, and the Zha'ertai-Bayan Obo-Huade and Yanliao basins at the northern margin (Fig. S-1). The Yanliao Basin is a typical intracratonic rift basin that extends from the northeastern end to the interior of the NCC. Geometrically, it can be divided into two branches: one oriented in a nearly northeast-east direction in the north and the other oriented in a nearly north-south direction in the south (Lu *et al.*, 2002; Deng *et al.*, 2021). However, the basin structure might have undergone a major change at *ca.* 1.6 Ga, connecting with the open sea in the north direction (Zhang *et al.*, 2021). The Xiamaling Formation (1.42–1.35Ga) was likely deposited in an offshore basin (Zhang *et al.*, 2019; Lyu *et al.*, 2021).

In the Yanliao Basin, the Paleo- and Mesoproterozoic sediments are found with a maximum thickness of up to 8000 m (Meng *et al.*, 2011). From bottom to top, these sediments can be classified as the clastic rock-dominated Changchengian System (including the Changzhougou, Chuanlinggou, Tuanshanzi, and Dahongyu formations), the carbonate rock-dominated Jixian System (including the Gaoyuzhuang, Yangzhuang, Wumishan, Hongshuizhuang, and Tieling formations), and the clastic-rock-dominated Xiamaling Formation (Fig. S-2). The duration and boundary ages of the Changchengian and Jixian systems, and the Xiamaling Formation have been well defined by using the U-Pb ages of zircons or baddeleyites from the ash layers, volcanic rocks and intrusive rocks (Fig. S-2).

The structural evolution and sedimentary sequences of the Yanliao Basin during 1.8–1.3 Ga are believed to be related to the breakup of the Columbia supercontinent (Deng *et al.*, 2021; Zhang *et al.*, 2021). Therefore, hydrothermal vents should have been active in a vicinity for an extended period of time. Evidence for hydrothermal contributions to basin geochemistry include the iron formation of the Chuanlinggou Formation (*ca.* 1640Ma) (Lin *et al.*, 2019), the manganese deposit and polymetallic pyrite deposit of the Gaoyuzhuang Formation (*ca.* 1590 Ma) (Gao *et al.*, 2021; Jin *et al.*, 2022), the syndepositional chert bands and nodules of the Wumishan Formation (*ca.* 1490 Ma) (Shen *et al.*, 2018), the black shale events of the Hongshuizhuang Formation (*ca.* 1460 Ma) (Ma *et al.*, 2017), and the iron formation of the Xiamaling Formation (Canfield *et al.*, 2018; Tang *et al.*, 2018). However, there is no direct evidence for the position of hydrothermal vents during the deposition of the Xiamaling iron formation.

The Xiamaling Formation

The Xiamaling Formation is mainly composed of shale and siltstone, and deposited over the carbonate rocks of the Tieling Formation with a parallel unconformity. Two zircon U-Pb TIMS ages (1384.4 ± 1.4 Ma and 1392.0 ± 1.0 Ma; Zhang *et al.*, 2015) and a zircon U-Pb LA-ICP-MS age (1418 ± 14 Ma; Lyu *et al.*, 2021) have been obtained from the volcanic ash layers in the middle and bottom of the Xiamaling Formation, respectively (Fig. S-3). In addition, abundant baddeleyite U-Pb ages of *ca.* 1320 Ma, obtained from the intruded gabbro-diorite sills (Li *et al.*, 2009; Liu *et al.*, 2011; Zhang *et al.*, 2017; Wang *et al.*, 2020), are considered to be accompanied by pre-magmatic uplift that started at about 1350 Ma (Zhang *et al.*, 2017), further constraining that the minimum age of the Xiamaling Formation should be older than 1350 Ma (Fig. S-2). Independent studies gave geological and paleogeographic evidence of an open system of the Yanliao Basin during the whole of the Xiamaling depositional period (Zhang *et al.*, 2019; Gao *et al.*, 2021; Wang *et al.*, 2020; Lyu *et al.*, 2021; Mitchell *et al.*, 2021).

Based on lithological characteristics, the Xiamaling Formation has been traditionally divided into four stratigraphic members in ascending order (*e.g.*, Tang *et al.*, 2018; Fig. S-3). Comparing the outcrop and core from the Xiahuayuan section (N $40^{\circ}28'13.41''$, E $115^{\circ}15'52.9''$), we have made a detailed geochemical and sedimentological investigation of the Xiamaling Formation (*e.g.*, Zhang *et al.*, 2015; Wang *et al.*, 2017; Canfield *et al.*, 2018; Zhang *et al.*, 2019), and have suggested a stratigraphic division scheme of 6 lithologic units (Fig. S-3). More detailed petrological and mineralogical descriptions of the Xiamaling iron formation can be seen in Canfield *et al.* (2018) and Tang *et al.* (2018).



Methods

Sample collection

All samples for geochemical analysis were obtained from a fresh drill core, where drilling was conducted with fresh water as the drilling fluid to minimise contamination. Fresh core samples were collected and crushed to powders with a diameter of <75 μm by using a tungsten carbide grinding disc.

Elemental measurements

Major and trace elements were determined at the Analytical Laboratory of Beijing Research Institute of Uranium Geology, China National Nuclear Corporation, after the methods described in [Zhang *et al.* \(2015\)](#). Briefly, major elements were determined using a Philips PW2400 X-ray fluorescence spectrometer (XRF). The relative standard deviations (RSD) of Fe and Al were both lower than 1.0 %. Trace elements were obtained on an ELEMENT XR inductively coupled plasma mass spectrometer (ICP-MS) after rock powders were subjected to complete digestion following the procedures described in [Zhang *et al.* \(2015\)](#). The resulting RSD of each rare earth element concentration was <1.5 %. Accuracies were also tested with the shale standard (GBW 03014) that was measured along with the samples. The concentrations of the interest elements were within 10 % of their reported values.

TOC measurement

Samples for TOC measurement were de-carbonated and combusted in a LECO CS-230HC carbon/sulphur analyser at the Key Laboratory of Petroleum Geochemistry, China National Petroleum Corporation and following the procedures described in [Canfield *et al.* \(2018\)](#). The resulting RSD of each sample was lower than 2.0 %.

Diagenetic minerals measurement

Diagenetic minerals of samples were determined through X-ray diffraction (XRD) analysis with a Rigaku MiniFlex X-ray diffractometer using a 600 W Cu- α source. The measurement were performed at the Key Laboratory of Petroleum Geochemistry, China National Petroleum Corporation and following procedures described in [Canfield *et al.* \(2018\)](#). The data were acquired through measurements of 10° per min over a range from 10° to 70° and analysed in the PDXL Software.

Carbon isotope measurement

Carbon isotopes of carbonate ($\delta^{13}\text{C}_{\text{carb}}$) and organic carbon ($\delta^{13}\text{C}_{\text{org}}$) of the samples were measured at the Key Laboratory of Petroleum Geochemistry, China National Petroleum Corporation and the University of Southern Denmark, after the methods described in [Canfield *et al.* \(2018\)](#). Briefly, pure kerogen was extracted from rocks through HCl and HF treatment as fully described in [Zhang *et al.* \(2016\)](#). The $\delta^{13}\text{C}_{\text{org}}$ values were measured on the extracted kerogens by using a Flush EA 1112 HT O/H-N/C combined with a Delta V Advantage mass spectrometer. The $\delta^{13}\text{C}_{\text{carb}}$ of each sample was determined by reacting with phosphoric acid in an online carbonate preparation device and analysis on a Finnigan Mat-252 mass spectrometer (Thermo Scientific). All $\delta^{13}\text{C}$ values were reported relative to the Vienna Pee Dee Belemnite (VPDB), with standard deviation (SD) of each sample was lower than 0.2 ‰ based on replicate analysis.

Extractable Fe^{2+} and Fe^{3+} analysis

We found that the standard iron speciation protocol ([Poulton and Canfield, 2005](#)) did not effectively extract the siderite in our samples due to their high contents. This was apparent as residues identifiable as siderite by XRD analysis were present after the “Fe carbonate” phase of the standard protocol. For this reason, we applied an HCl acid digestion procedure to these samples. This procedure involved reacting the samples overnight at 50 °C with 0.5 M HCl. This procedure was effective at removing both siderite and iron oxides from the sample. After extraction, samples were reacted with ferrozine to determine the Fe^{2+} contents.



Separate splits of each sample were also reacted with hydroxylamine to reduce Fe^{3+} to Fe^{2+} . This solution was reacted with ferrozine to yield total extractable iron, and the difference between the total extractable iron and the iron extracted as Fe^{2+} yielded the Fe^{3+} contents. This procedure was effective at removing iron from siderite and iron oxide-rich samples in the IF, but it might have also removed some silicate-bound iron in the clastic-rich samples. Analyses were conducted at the University of Southern Denmark. Details of the protocol used in partitioning between Fe^{2+} and Fe^{3+} can be found in [Viollier *et al.* \(2000\)](#).

Chromium reduction method

Pyrite sulphur was extracted by Cr reduction, trapped as Ag_2S , with concentrations calculated gravimetrically ([Canfield *et al.*, 1986](#)). Replicate extractions of PACS-2 and in-house standards indicated an analytical uncertainty of <5 %. These extractions were conducted at the University of Southern Denmark.

Iron isotope compositions analysis

The iron isotope compositions were measured at the Laboratory of Isotope Geology, Institute of Geology, Chinese Academy of Geological Sciences. The protocols used are briefly summarised here.

For iron isotope analyses, whole rock powders were digested with $\text{HF}+\text{HNO}_3+\text{HCl}+\text{HClO}_4$. After complete dissolution, the final solution was treated with concentrated HCl repeatedly to convert the cations to a chloride-form. The solution after HCl treatment was finally dissolved in 6 M HCl plus 0.001 % H_2O_2 for chemical purification of Fe^{3+} . The AG MP-1 anion exchange resin was used in the chromatographic separation procedure of Fe^{3+} . Samples were loaded and first washed with 6 M HCl plus 0.001% H_2O_2 to remove ions other than Fe^{3+} and Zn^{2+} , then 2 M HCl plus 0.001% H_2O_2 was used to strip Fe^{3+} from Zn^{2+} . Iron isotope ratios were determined in high mass resolution mode on a Nu Plasma high resolution multi-collector inductively coupled plasma mass spectrometer (HR MC-ICP-MS) using standard-sample bracketing (SSB) approach. Samples were introduced into the mass spectrometer in 0.1 M HNO_3 using a DSN 100 desolating nebulizer with 5 ppm Fe^{3+} . The $^{56}\text{Fe}/^{54}\text{Fe}$ ratio of each sample was reformulated into $\delta^{56}\text{Fe}$ -notation and expressed in units of per mille (‰), relative to the reference material of IRMM-014 as follows:

$$\delta^{56}\text{Fe} (\text{‰}) = \left[\frac{(^{56}\text{Fe}/^{54}\text{Fe})_{\text{sample}}}{(^{56}\text{Fe}/^{54}\text{Fe})_{\text{standard}}} - 1 \right] \times 1000 \quad (\text{Eq. S-1})$$

The long-term external reproducibility at high-resolution mode is better than 0.05 ‰ at 2 SD. Figure S-4 illustrates the relationship of $\delta^{56}\text{Fe}$ versus $\delta^{57}\text{Fe}$ ratios obtained for all Xiamaling samples. All the data lie on the mass-dependent fractionation line within analytical uncertainty.

Fe cycle and isotope systematics

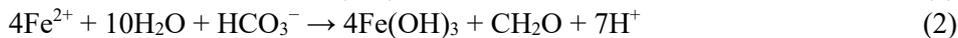
The sources of oceanic Fe^{2+} include hydrothermal fluids, the benthic shuttle from continental margins, and terrestrial input through riverine sources and aerosol deposition. Based on the compilations and models of [Condie \(1993\)](#), the average Fe_T/Al ratios of the Precambrian crust is taken to be 0.46, and average Fe_T/Ti is taken to be 11.23. These compositions would reflect the average detrital input to the ocean, ignoring biogeochemical diagenetic effects. Although riverine and aeolian sources of Fe might be important in the modern and Precambrian oceans, these terrestrial Fe inputs bear no obvious isotopic fractionations ($\Delta^{56}\text{Fe}_{\text{ferrous ion-total iron}}$) and probably had a minimal effect on the Fe isotope compositions ($\delta^{56}\text{Fe}$) of the Mesoproterozoic ferruginous marine waters ([Johnson *et al.*, 2020](#)). For hydrothermal and benthic Fe fluxes, atmospheric O_2 levels and marine sulfate-sulfide would have affected the Fe^{2+} oxidation extents in the oceans, the relative control of sulfides and oxides on isotopic exchange/fractionation with Fe^{2+} , and the Fe mass balances in the oceans. All of which could be recorded in the Fe composition and isotope values of sedimentary rocks.

Based on the modeling of [Kump and Seyfried \(2005\)](#), Precambrian hydrothermal fluids would have had much higher Fe/S ratios, with lower sulfide contents, and much higher Fe^{2+} contents. For the low O_2 and sulfate contents in the Mesoproterozoic ocean, especially in the deep ocean, the Fe^{2+} would have undergone minimal oxidation. Therefore, the $\square^{56}\text{Fe}$ of Fe^{2+} derived from distal hydrothermal plumes should have been preserved in transit to



continental margin basins. In the low-oxygen conditions of the Mesoproterozoic ocean, benthic Fe fluxes controlled by escape of pore fluid Fe^{2+} from marine sediments, might have been a very important source of Fe^{2+} (Raiswell and Canfield, 2012). The benthic Fe flux is also a function of the contents of reactive Fe^{3+} , organic carbon (C_{org}), and bottom-water O_2 . Sufficient delivery of reactive Fe^{3+} and C_{org} are needed to support dissimilatory iron reduction (DIR) and generate Fe^{2+} . Decreased Fe^{2+} oxidation in a low oxygen environment and decreased Fe^{2+} pyritisation in a low sulfide environment will increase the transport of diagenetic Fe^{2+} to water column.

The extremely negative $\delta^{13}\text{C}_{\text{carb}}$ values (from -27‰ to -8‰) of siderites from the XML IFs were suggested to have formed in 3 steps (Canfield *et al.*, 2018), including: 1) oxidation of seawater Fe^{2+} to Fe-oxyhydroxides ($\text{Fe}(\text{OH})_3$), likely at the chemocline of the ancient basin, 2) reduction of the $\text{Fe}(\text{OH})_3$ to diagenetic Fe^{2+} in the water column and sediments, and 3) crystallisation of Fe^{2+} as siderite. The $\text{Fe}(\text{OH})_3$ in step 1 can form either through the oxidation of seawater Fe^{2+} with O_2 (Eq. 1) or from anoxygenic photosynthesis at the chemocline (Eq. 2). Step 1 generates ^{56}Fe -enriched Fe-(oxy)hydroxides with an abiotic $\Delta^{56}\text{Fe}_{\text{hydroxide-ferrous ion}}$ of *ca.* $+3.0$ or biotic $\Delta^{56}\text{Fe}_{\text{hydroxide-ferrous ion}}$ from $+1.5\text{‰}$ to $+3.0\text{‰}$ (Johnson *et al.*, 2020). Step 2 can occur both in the seawater and in the pore-waters, and generates ^{56}Fe -depleted diagenetic Fe^{2+} (Eq. 3) with a similar $\Delta^{56}\text{Fe}_{\text{ferrous ion-hydroxide}}$ of *ca.* -3.0‰ through abiotic or biotic pathways (Johnson *et al.*, 2020). Step 3 occurs in the sediment and generates ^{56}Fe -depleted siderite (Eq. 4) with a $\Delta^{56}\text{Fe}_{\text{ferrous ion-siderite}}$ of -0.5‰ in the abiotic system (Wiesli *et al.*, 2004).



Calculation of the clastic and diagenetic siderite end-members using iron isotope mass balance

Whole rock $\delta^{56}\text{Fe}$ reflect the net Fe isotopic composition of a mixture of different iron-bearing minerals, whose contents and isotopic compositions vary between samples. For the siderite-dominated Xiamaling Iron Formation, the contents of Fe-oxides and pyrite are much lower than siderite. So, clastic Fe and diagenetic siderite were assumed to be the two main endmembers that affect the whole rock $\delta^{56}\text{Fe}$. A simple mixing model was used to calculate the evolution of $\delta^{56}\text{Fe}$ by mixing between clastic and diagenetic endmembers, whose $\delta^{56}\text{Fe}$ were also refined in the modelling. In our model, the whole rock $\delta^{56}\text{Fe}$ was defined to be:

$$\delta^{56}\text{Fe}_{\text{wh}} = (\text{Fe}_{\text{cla}} \times \delta^{56}\text{Fe}_{\text{cla}} + \text{Fe}_{\text{dia}} \times \delta^{56}\text{Fe}_{\text{dia}}) / (\text{Fe}_{\text{cla}} + \text{Fe}_{\text{dia}}) \quad (\text{Eq. S-2})$$

Here, $\delta^{56}\text{Fe}_{\text{wh}}$, $\delta^{56}\text{Fe}_{\text{cla}}$ and $\delta^{56}\text{Fe}_{\text{dia}}$ are iron isotopic values of whole rock, clastic endmember and diagenetic endmember, respectively. Fe_{cla} and Fe_{dia} are the iron amounts in the clastic and diagenetic endmembers, respectively. The sum of Fe_{cla} and Fe_{dia} is total Fe (Fe_T).

$$\text{Fe}_T = \text{Fe}_{\text{cla}} + \text{Fe}_{\text{dia}} \quad (\text{Eq. S-3})$$

Fe_{cla} and Fe_{dia} can be further defined as:

$$\text{Fe}_{\text{cla}} = f_{\text{cla-Fe}} \times T_{\text{cla-Fe}} \quad (\text{Eq. S-4})$$

$$\text{Fe}_{\text{dia}} = f_{\text{dia-Fe}} \times T_{\text{dia-Fe}} \quad (\text{Eq. S-5})$$

Here, $f_{\text{cla-Fe}}$ and $f_{\text{dia-Fe}}$ are the fractions of clastic endmember and diagenetic endmember, respectively. $T_{\text{cla-Fe}}$ and $T_{\text{dia-Fe}}$ are iron contents of the clastic endmember and diagenetic endmember, respectively. The sum of $f_{\text{cla-Fe}}$ and $f_{\text{dia-Fe}}$ is 1.



Then, Equation S-2 can be transformed into:

$$\delta^{56}\text{Fe}_{\text{wh}} = T_{\text{cla-Fe}} \times T_{\text{dia-Fe}} \times (\delta^{56}\text{Fe}_{\text{cla}} - \delta^{56}\text{Fe}_{\text{dia}}) / (T_{\text{dia-Fe}} - T_{\text{cla-Fe}}) / \text{Fe}_{\text{T}} + (T_{\text{dia-Fe}} \times \delta^{56}\text{Fe}_{\text{dia}} - T_{\text{cla-Fe}} \times \delta^{56}\text{Fe}_{\text{cla}}) / (T_{\text{dia-Fe}} - T_{\text{cla-Fe}}) \quad (\text{Eq. S-5})$$

So, we can use the formula $Y = a/x + b$ to do the optimal fitting between $\delta^{56}\text{Fe}_{\text{wh}}$ and Fe_{T} , with

$$a = T_{\text{cla-Fe}} \times T_{\text{dia-Fe}} \times (\delta^{56}\text{Fe}_{\text{cla}} - \delta^{56}\text{Fe}_{\text{dia}}) / (T_{\text{dia-Fe}} - T_{\text{cla-Fe}}) \quad (\text{Eq. S-6})$$

$$b = (T_{\text{dia-Fe}} \times \delta^{56}\text{Fe}_{\text{dia}} - T_{\text{cla-Fe}} \times \delta^{56}\text{Fe}_{\text{cla}}) / (T_{\text{dia-Fe}} - T_{\text{cla-Fe}}) \quad (\text{Eq. S-7})$$

With a $T_{\text{cla-Fe}}$ of 3.6 % (upper crust value; Rudnick and Gao, 2003) and $T_{\text{dia-Fe}}$ of 48 %, the $\delta^{56}\text{Fe}_{\text{cla}}$ and $\delta^{56}\text{Fe}_{\text{dia}}$ can be calculated with the optimised a and b values.

Supplementary Table

Table S-1 Geochemical data of the Xiamaling Iron Formation.

Table S-1 is available for download (Excel file) from the online version of the article at <https://doi.org/10.7185/geochemlet.2208>.



Supplementary Figures

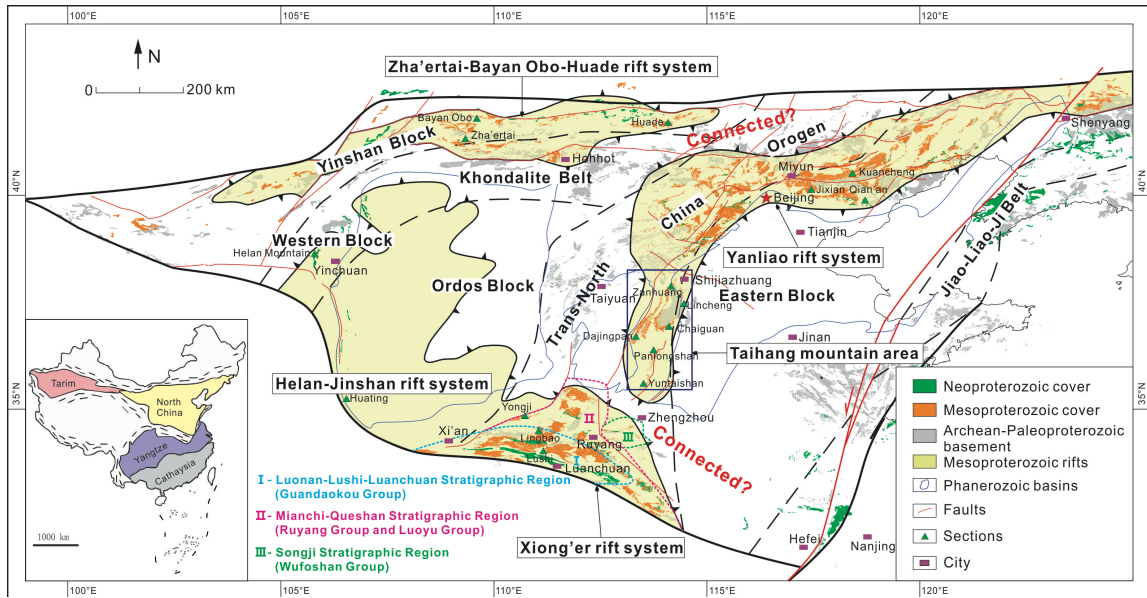


Figure S-1 Distributions of the Proterozoic rift systems (basins) and sedimentary covers in the North China Craton. Modified from [Deng et al. \(2021\)](#).

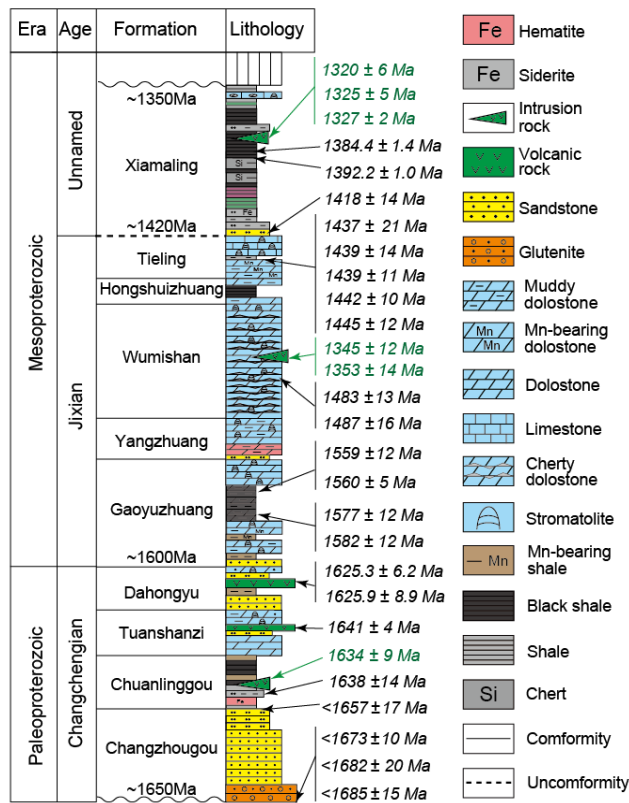


Figure S-2 The Palaeo- and Mesoproterozoic stratigraphic framework and U-Pb ages of zircons or baddeleyites from the ash layers, volcanic rocks and intrusive rocks in the Yanliao Basin, North China Craton. Modified from [Zhang et al. \(2021\)](#).

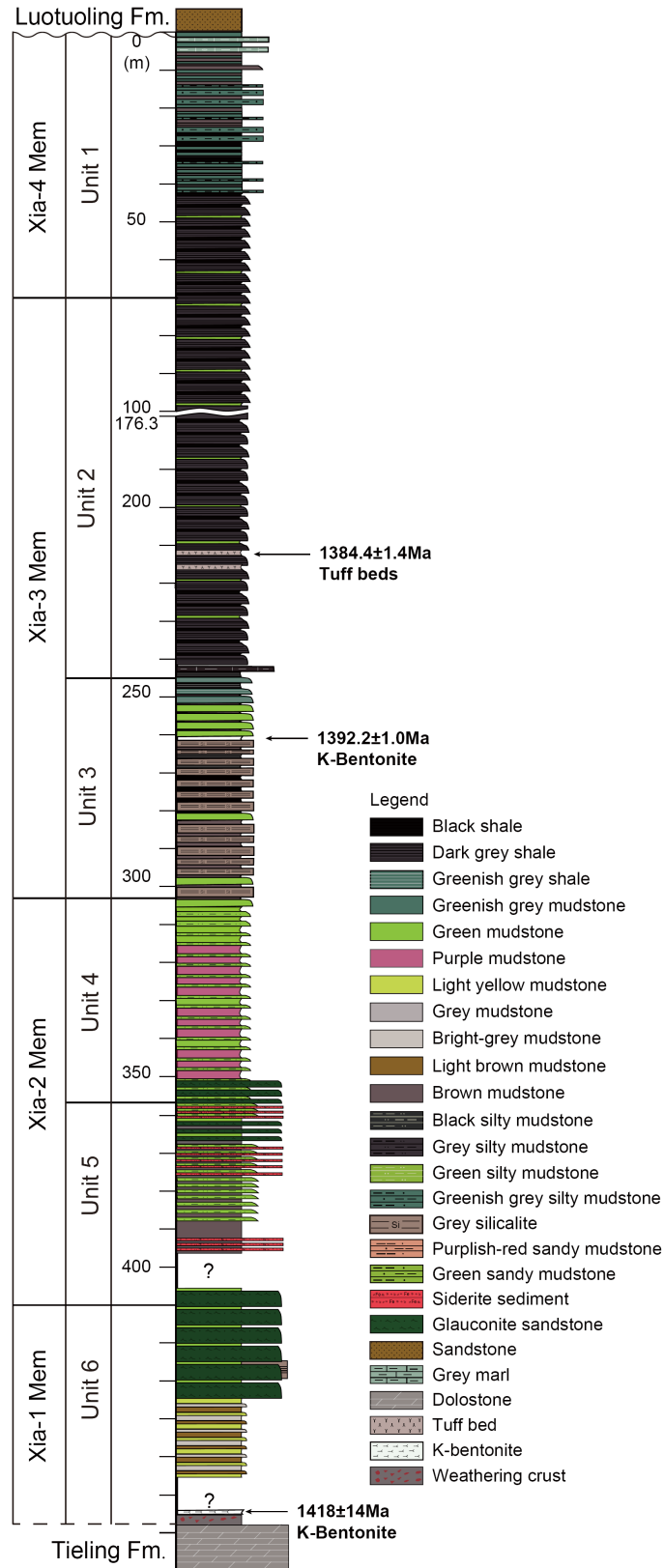


Figure S-3 The stratigraphic column of the Xiamaling Formation in the Yanliao Basin, North China Craton, modified from Zhang *et al.* (2019). The age of 1418 ± 14 Ma is from Lyu *et al.* (2021).



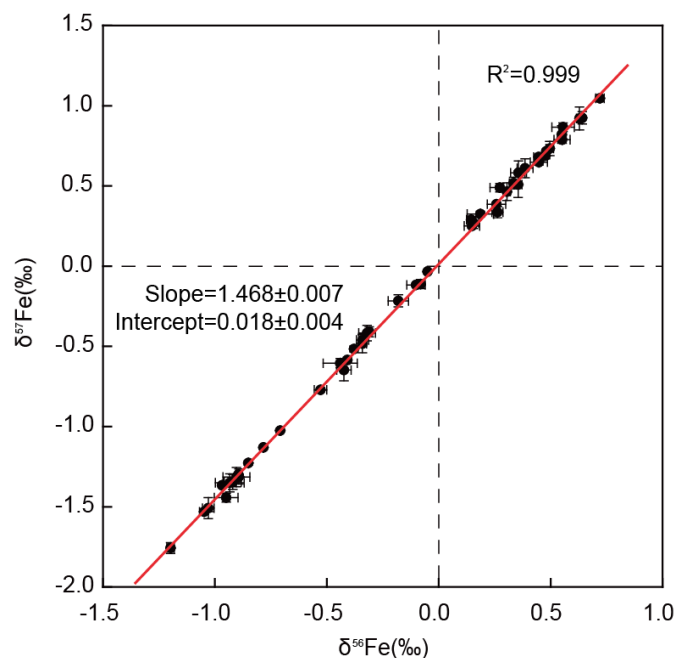


Figure S-4 $\delta^{56}\text{Fe}$ versus $\delta^{57}\text{Fe}$ of the Xiamaling samples normalised by IRMM-014. The red line is the theoretical mass-dependent fractionation line (slope = 1.474) based on a simple harmonic oscillator approximation (Criss, 1999).

Supplementary Information References

- Canfield, D.E., Raiswell, R., Westrich, J.T., Reaves, C.M., Berner, R.A. (1986) The use of chromium reduction in the analysis of reduced inorganic sulfur in sediments and shales. *Chemical Geology* 54, 149–155. [https://doi.org/10.1016/0009-2541\(86\)90078-1](https://doi.org/10.1016/0009-2541(86)90078-1)
- Canfield, D.E., Zhang, S.C., Wang, H.J., Wang, X.M., Zhao, W.Z., Su, J., Bjerrum, C.J., Haxen, E.R., Hammarlund, E.U. (2018) A Mesoproterozoic Iron Formation. *Proceedings of the National Academy of Sciences of the United States of America* 115, E3895–E3904. <https://doi.org/10.1073/pnas.1720529115>
- Condie, K.C. (1993) Chemical composition and evolution of the upper continental crust: contrasting results from surface samples and shales. *Chemical Geology* 104, 1–37. [https://doi.org/10.1016/0009-2541\(93\)90140-E](https://doi.org/10.1016/0009-2541(93)90140-E)
- Criss, R.E. (1999) *Principles of Stable Isotope Distribution*. Oxford University Press, New York. <https://doi.org/10.1093/oso/9780195117752.001.0001>
- Deng Y., Wang H.J., Lyu D., Zhang F.L., Gao, Z.Y., Ren, R., Ye, T.T., Lyu, Y.T., Wang, X.M., Guan, P., Zhang, S.C. (2021) Evolution of the 1.8–1.6 Ga Yanliao and Xiong'er basins, north China Craton. *Precambrian Research* 365, 106383. <https://doi.org/10.1016/j.precamres.2021.106383>
- Gao, B.Y., Zhang, L.C., Jin, X.D., Li, Z.Q., Li, W.J. (2020) Rhenium-Osmium isotope systematics of an Early Mesoproterozoic SEDEX polymetallic pyrite deposit in the North China Craton: Implications for geological significance and the marine osmium isotopic record. *Ore Geology Reviews* 117, 103331. <https://doi.org/10.1016/j.oregeorev.2020.103331>
- Gao, Z.Y., Wang, H.J., Feng, J.R., Luo, Z., Zhang, Y.H., Li, X.H. (2021) Provenance and paleogeographic environment of the Middle Proterozoic Xiamaling formation in Yanliao Basin. *Acta Geologica Sinica* 95, 3606–3628. <http://doi.org/10.19762/j.cnki.dizhixuebao.2020289>. (in Chinese with English abstract)
- Jia, X.L., Zhai, M.G., Xiao, W.J., Sun, Y., Ratheesh-Kumar, R.T., Yang, H., Zhou, K.F., Wu, J.L. (2019) Late Neoproterozoic to early Paleoproterozoic tectonic evolution of the southern North China Craton: Evidence from geochemistry, zircon geochronology and Hf isotopes of felsic gneisses from the Taihua complex.

Precambrian Research 326, 222–239. <https://doi.org/10.1016/j.precamres.2017.11.013>

- Jin, S., Ma, P., Guo, H., Yu, W.C., Xu, L.T., Lin, Q. (2022) Genesis of Mesoproterozoic Gaoyuzhuang Formation manganese ore in Qinjiayu, East Hebei: Constraints from mineralogical and geochemical evidences. *Earth Science*, 47, 277–289. <https://doi.org/10.3799/dqkx.2021.055> (in Chinese with English abstract)
- Johnson, C., Beard, B., Weyer, S. (2020) *Iron Geochemistry: An Isotopic Perspective*. Springer Nature Press, Switzerland AG. <https://doi.org/10.1007/978-3-030-33828-2>
- Kump, L.R., Seyfried, W.E. (2005) Hydrothermal Fe fluxes during the Precambrian: effect of low oceanic sulfate concentrations and low hydrostatic pressure on the composition of black smokers. *Earth and Planetary Science Letters* 235, 654–662. <https://doi.org/10.1016/j.epsl.2005.04.040>
- Li, H.K., Lu, S.N., Li, H.M., Sun, L.X., Xiang, Z.Q., Geng, J.Z., Zhou, H.Y. (2009) Zircon and beddeleyite U-Pb precision dating of basic rock sills intruding Xiamaling Formation, North China. *Geological Bulletin of China* 28, 1396–1404. (in Chinese with English abstract)
- Li, S.Z., Li, X.Y., Wang, G.Z., Liu, Y.M., Wang, Z.C., Wang, T.S., Cao, X.Z., Guo, X.Y., Somerville, I., Li, Y., Zhou, J., Dai, L.M., Jiang, S.H., Zhao, H., Wang, Y., Wang, G., Yu, S. (2020) Global Meso-Neoproterozoic plate reconstruction and formation mechanism for Precambrian basins: constraints from three cratons in China. *Earth-Science Reviews* 198, 102946. <https://doi.org/10.1016/j.earscirev.2019.102946>
- Lin, Y.T., Tang, D.J., Shi, X.Y., Zhou, X.Q., Huang, K.J. (2019) Shallow-marine ironstones formed by microaerophilic iron-oxidizing bacteria in terminal Paleoproterozoic. *Gondwana Research* 76, 1–18. <https://doi.org/10.1016/j.gr.2019.06.004>
- Liu, Y., Zhong, N.N., Tian, Y.J., Qi, W., Mu, G.Y. (2011) The oldest oil accumulation in China: Meso-proterozoic Xiamaling Formation bituminous sandstone reservoirs. *Petroleum Exploration and Development* 38, 503–512. [https://doi.org/10.1016/S1876-3804\(11\)60050-5](https://doi.org/10.1016/S1876-3804(11)60050-5)
- Lu, S.N., Yang, C.L., Li, H.K., Li, H.M. (2002) A group of rifting events in the terminal paleoproterozoic in the North China Craton. *Gondwana Research* 5, 123–131. [https://doi.org/10.1016/S1342-937X\(05\)70896-0](https://doi.org/10.1016/S1342-937X(05)70896-0)
- Lyu, D., Deng, Y., Wang, H.J., Zhang, F.L., Ren, R., Gao, Z.Y., Zhou, C.M., Luo, Z., Wang, X.M., Bi, L.N., Zhang, S.C., Canfield, D.E. (2021) Using cyclostratigraphic evidence to define the unconformity caused by the Mesoproterozoic Qinyu Uplift in the North China Craton. *Journal of Asian Earth Sciences* 206, 104608. <https://doi.org/10.1016/j.jseaes.2020.104608>
- Ma, K., Hu, S.Y., Wang, T.S., Zhang, B.M., Qin, S.F., Shi, S.Y., Wang, K., Huang, Q.Y., (2017) Sedimentary environments and mechanisms of organic matter enrichment in the Mesoproterozoic Hongshuizhuang Formation of northern China. *Palaeogeography, Palaeoclimatology, Palaeoecology* 475, 176–187. <https://doi.org/10.1016/j.palaeo.2017.02.038>
- Meng, Q.R., Wei, H.H., Qu, Y.Q., Ma, S.X. (2011) Stratigraphic and sedimentary records of the rift to drift evolution of the Northern North China Craton at the Paleo- to Mesoproterozoic transition. *Gondwana Research* 20, 205–218. <https://doi.org/10.1016/j.gr.2010.12.010>
- Mitchell, R.N., Kirscher, U., Kunzmann, M., Liu, Y., Cox, G.M. (2021) Gulf of Nuna: Astrochronologic correlation of a Mesoproterozoic oceanic euxinic event. *Geology* 49, 25–29. <https://doi.org/10.1130/G47587.1>
- Pisarevsky, S.A., Elming, S.Å., Pesonen, L.J., Li, Z.X. (2014) Mesoproterozoic paleogeography: supercontinent and beyond. *Precambrian Research* 244, 207–225. <https://doi.org/10.1016/j.precamres.2013.05.014>
- Poulton, S.W., Canfield, D.E. (2005) Development of a sequential extraction procedure for iron: implications for iron partitioning in continentally derived particulates. *Chemical Geology* 214, 209–221. <https://doi.org/10.1016/j.chemgeo.2004.09.003>
- Raiswell, R., Canfield, D.E. (2012) The Iron Biogeochemical Cycle Past and Present. *Geochemical Perspectives* 1, 1–220. <https://doi.org/10.7185/geochempersp.1.1>
- Rudnick, R.L., Gao, S. (2003) Composition of the continental crust. In: Holland, H.D., Turekian, K.K. (Eds.) *Treatise on Geochemistry*. Elsevier-Pergamon, Oxford, 1–64. <https://doi.org/10.1016/B0-08-043751-6/03016-4>



- Shen, B., Ma H.R., Ye, H.Q., Lang, X.G., Pei, H.X., Zhou, C.M., Zhang, S.H., Yang, R.Y. (2018) Hydrothermal origin of syndepositional chert bands and nodules in the Mesoproterozoic Wumishan Formation: Implications for the evolution of Mesoproterozoic cratonic basin, North China. *Precambrian Research* 310, 213–228. <https://doi.org/10.1016/j.precamres.2018.03.007>
- Tang, D.J., Shi, X.Y., Jiang, G.Q., Wu, T., Ma, J.B., Zhou, X.Q. (2018) Stratiform siderites from the Mesoproterozoic Xiamaling Formation in North China: Genesis and environmental implications. *Gondwana Research* 58, 1–15. <https://doi.org/10.1016/j.gr.2018.01.013>
- Viollier, E., Inglett, P.W., Hunter, K., Roychoudhury, A.N., Cappellen, P.V. (2000) The ferrozine method revisited: Fe(II)/Fe(III) determination in natural waters. *Applied Geochemistry* 15, 785–790. [https://doi.org/10.1016/S0883-2927\(99\)00097-9](https://doi.org/10.1016/S0883-2927(99)00097-9)
- Wang, H.Y., Zhang, Z.H., Li, C., Algeo, T.J., Cheng, M., Wang, W. (2020) Spatiotemporal redox heterogeneity and transient marine shelf oxygenation in the Mesoproterozoic ocean. *Geochimica et Cosmochimica Acta* 270, 201–217. <https://doi.org/10.1016/j.gca.2019.11.028>
- Wang, X.M., Zhang, S.C., Wang, H.J., Bjerrum, C.J., Hammarlund, E.U., Haxen, E.R., Su, J., Wang, Y., Canfield, D.E. (2017) Oxygen, climate and the chemical evolution of a 1400 million years old tropical marine setting. *American Journal of Science* 317, 861–900. <https://doi.org/10.2475/08.2017.01>
- Wiesli, R.A., Beard, B.L., Johnson, C.M. (2004) Experimental determination of Fe isotope fractionation between aqueous Fe(II), siderite and “green rust” in abiotic systems. *Chemical Geology* 211, 343–362. <https://doi.org/10.1016/j.chemgeo.2004.07.002>
- Zhang, S.C., Wang, X.M., Hammarlund, E.U., Wang, H.J., Costa, M.M., Bjerrum, C.J., Connelly, J.N., Zhang, B.M., Bian, L.Z., Canfield, D.E. (2015) Orbital forcing of climate 1.4 billion years ago. *Proceedings of the National Academy of Sciences of the United States of America* 112, 1406–1413. <https://doi.org/10.1073/pnas.1502239112>
- Zhang, S.C., Wang, X.M., Wang, H.J., Bjerrum, C.J., Hammarlund, E.U., Costa, M.M., Connelly, J.N., Zhang, B.M., Su, J., Canfield, D.E. (2016) Sufficient oxygen for animal respiration 1,400 million years ago. *Proceedings of the National Academy of Sciences of the United States of America* 113, 1731–1736. <https://doi.org/10.1073/pnas.1523449113>
- Zhang, S.C., Wang, X.M., Wang, H.J., Bjerrum, C.J., Hammarlund, E.U., Haxen, E.R., Wen, H.J., Ye, Y.T., Canfield, D.E. (2019) Paleoenvironmental proxies and what the Xiamaling Formation tells us about the mid-Proterozoic ocean. *Geobiology* 17, 225–246. <https://doi.org/10.1111/gbi.12337>
- Zhang, S.C., Wang, H.J., Wang, X.M., Ye, Y.T. (2021) The Mesoproterozoic Oxygenation Event. *Science China: Earth Science* 64. <https://doi.org/10.1007/s11430-020-9825-x>
- Zhang, S.H., Zhao, Y., Li, X., Ernst, R. E., Yang, Z. (2017) The 1.33–1.30 Ga Yanliao large igneous province in the North China Craton: Implications for reconstruction of the Nuna (Columbia) supercontinent, and specifically with the North Australian Craton. *Earth and Planetary Science Letters* 465, 112–125. <https://doi.org/10.1016/j.epsl.2017.02.034>
- Zhao, G.C., Zhai, M.G. (2013) Lithotectonic elements of precambrian basement in the North China Craton: review and tectonic implications. *Gondwana Research* 23, 1207–1240. <https://doi.org/10.1016/j.gr.2012.08.016>
- Zhu, Y.S., Yang, J.H., Wang, H.; Wu, F.Y. (2020) Mesoproterozoic (~1.32 Ga) modification of lithospheric mantle beneath the North China craton caused by break-up of the Columbia supercontinent. *Precambrian Research* 2020, 342, 105674. <https://doi.org/10.1016/j.precamres.2020.105674>

